Interatomic potential for predicting the thermal conductivity of zirconium trisulfide monolayers with molecular dynamics

Interatomic Potential for Predicting the Thermal Conductivity of Zirconium Trisulphide Monolayers with Molecular Dynamics

Fernan Saiz,[1, a)] Yenal Karaaslan,[2, b)] Riccardo Rurali,[1, c)] and Cem Sevik[2, 3, d)]
[1)] *Institut de Ciència de Materials de Barcelona (ICMAB–CSIC)*
Campus de Bellaterra, 08193 Bellaterra, Barcelona, Spain
[2)] *Department of Mechanical Engineering, Faculty of Engineering, Eskişehir Technical University, 26555, Eskişehir, Turkey*
[3)] *Department of Physics, University of Antwerp, 2020 Antwerp, Belgium*

(Dated: 29 April 2021)

We present here a new interatomic potential parameter set to predict the thermal conductivity of zirconium trisulphide monolayers. The generated Tersoff type force field is parameterized using data collected with first-principles calculations. We use non-equilibrium molecular dynamics simulations to predict the thermal conductivity. The generated parameters result in very good agreement in structural, mechanical, and dynamical parameters. The room temperature lattice thermal conductivity (κ) of the considered crystal is predicted to be κ_{xx} = 25.69 W m^{-1} K^{-1} and κ_{yy} = 42.38 W m^{-1} K^{-1}, which both agree well with their corresponding first-principles values, with a discrepancy of less than 5%. Moreover, the calculated κ variation with temperature (200 and 400 K) are comparable within the framework of the accuracy of both first-principles and molecular dynamics simulations.

I. INTRODUCTION

The discovery of graphene[1,2] has spanned the synthesis of a large number of new two-dimensional materials such as boron nitride (h-BN), silicene, black phosphorus, transition metal oxides, and transition metal dichalcogenides. The idea behind making a compound with the thickness of one atomic layer is to exploit its enhanced mechanical, electronic and thermal transport properties with respect to those exhibited by its bulk counterpart. For example, while graphite has a finite electronic band gap, graphene has no band gap[3] as well as a much higher thermal conductivity[4] by one order of magnitude. Moreover, many of these new 2D materials have different properties than graphene. For instance, the monolayers of some transition metal dichalcogenides, such as MoS_2 and WS_2, exhibit direct band gaps, making them ideal for a wide range of applications in electronics and optoelectronics.[5,6]

Currently, additional efforts are being made to investigate a new class of chalcogenides with formula MX_3, where M = Ti, Zr, or Hf and X = S, Se, or Te,[7,8]. These trichalcogenides have recently attracted much attention due to their narrow band gaps between 1.0 and 2.0 eV[9] that make their nanosheets suitable not only for optical and electronic applications,[10] but also for building thermoelectric devices[11–13]. For thermoelectric applications, the aim is always to increase the efficiency of the material of interest, which is governed by the figure of merit

$$zT = \frac{S^2\sigma}{\kappa_{el} + \kappa_{ph}} T, \tag{1}$$

where T is the temperature, S is the thermopower or Seebeck coefficient, σ is the electrical conductivity, and κ_{el} and κ_{ph} are the electronic and phononic contributions to the thermal conductivity, respectively. Hence, the figure of merit can be improved by either increasing the electronic transport properties (S and σ) or decreasing the thermal transport (κ_{el} and κ_{ph}). To this end, a number of strategies have been put into action such as assembling superlattices[14,15] or applying strain[13]. Nonetheless, the calculation of these properties requires using quantum-mechanical codes that solve the Schrödinger equation. In particular, the computation of the phononic thermal conductivity using first-principles lattice dynamics in monolayers is very costly[16,17]. For instance, materials whose unit cells are composed of a few atoms require hundreds of simulations based on density functional theory (DFT) to build the matrices of second and third order force constants that are used in turn to compute the thermal conductivity tensor. Therefore, it is desirable that this tensor can be obtained with cheaper computational techniques, such as classical molecular dynamics (MD), that are faster -sand more versatile —allowing, for instance, for nanostructuring— than first-principles lattice dynamics.

The goal of this work is then to calculate the components of the thermal conductivity tensor κ_{xx} and κ_{yy} in ZrS_3 monolayers with MD simulations. The accuracy of MD depends on the potential energy function $V(r)$ determined at a given position r that is differentiated to find the forces $f(r)$ acting on the constituent particles of the system. These forces are then used to integrate the equations of motion at each time step, which allows tracking the atomic trajectories throughout the simulation. Therefore, the starting point of this work is to build a potential energy function by fitting its parameters to the phonon dispersion curves obtained with first-principles lattice dynamics. We then produce several sets of parameters to find the one

[a)]Electronic mail: ORCiD: 0000-0001-8565-8044
f.saiz@csic.es
[b)]Electronic mail: ORCiD: 0000-0001-8483-4819
yenalkaraaslan@gmail.com
[c)]Electronic mail: ORCiD: 0000-0002-4086-4191
rrurali@icmab.es
[d)]Electronic mail: ORCiD: 0000-0002-2412-9672
csevik@eskisehir.edu.tr

that predicts the thermal conductivity components κ_{xx} and κ_{yy} in best agreement with DFT's. These MD components are determined using the non-equilibrium method,[18,19] in which a heat flux is imposed on one direction of the monolayer and the system's response is a thermal gradient, which allows to determine the thermal conductivity components using Fourier's law. Another popular method to calculate these two components is the Green-Kubo method,[20,21] which is based on the fluctuation-dissipation theorem applied on the heat autocorrelation function that establishes a link to determine the thermal conductivity. However, it can be argued that when applied to monolayers with a very low thermal conductivity such as ZrS_3, this method is inappropriate because it produces averaged values accompanied with standard deviations of the same order of magnitude, presenting thus the final results with a high uncertainty.[22] This uncertainty is specially critical, as in this paper we are not only interested in qualitatively matching the DFT components of the phononic thermal conductivity, but also in obtaining the anisotropy (i.e. $\kappa_{yy}/\kappa_{xx} \neq 1$) for ZrS_3, a property common to other trichalcogenides[17,23].

After this introduction, this manuscript is organized as follows: in Sec. II we describe the recipe used to make our first-principles calculations, starting from the geometry optimisations of the ZrS_3 systems to the calculation of the thermal properties with lattice dynamics. We explain the fitting procedure to generate the parameters for the interatomic potential and the setup of the non-equilibrium MD simulations. Next, in Sec. III we compare the phonon dispersions of ZrS_3 with DFT and MD, present the thermal conductivities obtained with both methods, and analyze other thermal transport properties. Finally, Sec. IV concludes with our main findings and implications of this work.

II. THEORETICAL METHODS

A. First-principles calculations

Our methodology starts by employing the Vienna Ab initio Package (VASP)[24–27] to relax the atomic positions and cell parameters of these nanosheets. The monolayers are first represented as a unit cell belonging to the $P2_1/m$ space group as shown in Figure 1. Reciprocal space integrations are made using a mesh of $10 \times 14 \times 1$ **k**-points centered at Γ in the Brillouin zone. The geometry relaxation is carried out setting thresholds of 1×10^{-6} eV/nm for the forces and 1×10^{-8} eV for the self-consistency solution of the wavefunction. We use the generalized gradient approximation of the exchange-correlation potential in the Perdew-Burke-Ernzerhof (PBE) flavour[28] and the projector augmented wave method (PAW)[29,30]. We expand the valence orbitals with a plane wave basis with an energy cutoff of 350 eV. Long-range van der Waals forces are included using the zero damping Grimme's DFT-D3 scheme. Once the geometry of the ZrS_3 monolayer is optimized, we obtain the following parameters for the monolayer a = 0.512 nm and b = 0.363 nm with a residual value for the external pressure of -0.30 kbar. As a reference, bulk values from Ref.[8] are a = 0.512 nm and b = 0.362 nm.

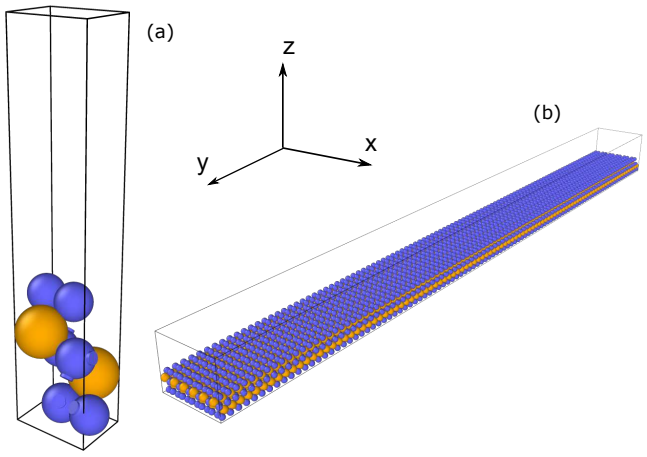

FIG. 1. Representation of a ZrS_3 unit cell (a) and a supercell made of 6x100x1 replicas of the former (b) with atoms painted in orange for zirconium and in blue for sulfur as well.

Starting from the optimized primitive cell, we compute the interatomic force constants (IFCs) in 4×5 supercells using the finite differences method. For the harmonic displacements we use the PHONOPY code[31] considering all neighboring interactions. THIRDORDER.PY[32,33] is used to characterize the anharmonic interactions, neglecting those beyond seventh neighbors. The IFCs are then used as an input to solve the Boltzmann Transport Equation (BTE) iteratively with the almaBTE code[34] and the lattice thermal conductivity is obtained as

$$\kappa_{ij} = \sum_{\lambda} \kappa_{ij,\lambda} = C \sum_{\lambda} f_{\lambda}(f_{\lambda}+1)(h\nu_{\lambda})^2 v_{i,\lambda} F_{j,\lambda}, \qquad (2)$$

where i and j are the spatial directions x, y, and z, $C^{-1} = k_B T^2 \Omega N$ being k_B Boltzmann's constant, h the Planck's constant, Ω the unit cell's volume, and N the number of **q**-points. The summation in Eq. 2 runs over all phonon modes λ; each mode has a frequency ν_{λ} and a group velocity $\mathbf{v}_{\lambda}$, and at thermal equilibrium at temperature T its occupancy follows the Bose-Einstein distribution f_{λ}. The mean free displacement is initially calculated as $F_{j,\lambda} = \tau_{\lambda} v_{j,\lambda}$, where τ_{λ} is the lifetime of mode λ within the relaxation time approximation (RTA). Starting from this guess, the solution is then obtained iteratively and $F_{j,\lambda}$ takes the general form $\tau_{\lambda}(v_{j,\lambda} + \Delta_{j,\lambda})$, where the correction Δ_{λ} captures the changes in the heat current associated to the deviations in the phonon populations computed at the RTA level[35,36]. Scattering from isotopic disorder is also included considering the natural distributions of Zr and S isotopes within Tamura's model[37]. Given that we use periodic boundary conditions and the corresponding breakdown of continuous rotation symmetry, the phonon frequencies of 2D systems calculated using this method are known to include numerical error that can lead to the appearance of artificial imaginary acoustic frequencies near Γ.[16,17,38] Therefore, we apply a correction[38] to enforce the rotational symmetry in our calculations.

B. Parameterization of the force field

Our empirical interatomic potential (EIAP) for ZrS_3 monolayers takes the classical Tersoff[39] form

$$V_{ij}(r_{ij}) = f_C(r_{ij})\left[f_R(r_{ij}) + b_{ij} f_A(r_{ij})\right], \tag{3}$$

where the functions f's are defined as follows

$$\begin{aligned}
f_C(r) &= \begin{cases} 1 & : \quad r < R-D \\ \frac{1}{2} - \frac{1}{2}\sin\left(\frac{\pi}{2}\frac{r-R}{D}\right) & : \quad R-D < r < R+D \\ 0 & : \quad r > R+D \end{cases} \\
f_R(r) &= A\exp(-\lambda_1 r), \\
f_A(r) &= -B\exp(-\lambda_2 r), \\
b_{ij} &= \left(1+\beta^n {\zeta_{ij}}^n\right)^{-\frac{1}{2n}}, \\
\zeta_{ij} &= \sum_{k\neq i,j} f_C(r_{ik}) g(\theta_{ijk}) \exp\left[{\lambda_3}^3 (r_{ij}-r_{ik})^3\right], \\
g(\theta_{ijk}) &= 1 + \frac{c^2}{d^2} - \frac{c^2}{\left[d^2 + (h-\cos\theta_{ijk})^2\right]}.
\end{aligned} \tag{4}$$

The functions f's depend on the two-body interatomic distance r_{ij} between the atom i and its neighbor j. f_R is the repulsive potential energy function, f_A is the attractive potential energy function. The parameter b_{ij} depend on two- and three-body interactions that take the distances r_{ij} and r_{ik} and the angle θ_{ijk}. The pairwise separation r_{ik} is taken between the atom i and its neighbor k. Both distances are then taken to determine the angle θ_{ijk} with the particle i as the central atom. f_C is a smooth cutoff function that limits the range of the potential over the nearest-neighbor interactions within a cutoff distance, $R+D$.

Considering the atoms within the cutoff distance by R and D, two-body parameters, A, B, λ_1, λ_2 for S-S interactions, and both two-body (A, B, λ_1, λ_2) and desired three-body (λ_3, n, β, c, d, h) parameters for Zr-S (Zr-S-S, and S-Zr-Zr) interactions are obtained through the particle swarm optimization (PSO) method[40–43]. For this purpose, the fitness function for the PSO

$$f(x) = \sum_{i=1}^{I} \frac{d_i - a_i}{d_i}, \tag{5}$$

where d_i points out the desired value of the characteristic i obtained by first-principles calculations, a_i points out the actual value of the characteristic i obtained via the empirical potential for a given set of parameters, and $I = 10^3$ is the total number of the certain physical characteristics of crystal to be optimized simultaneously. These characteristics are two lattice constants, ninety-three phonon frequencies corresponding to the selected acoustic (and optic) vibrations for three (and four) different wavelengths, eight total energy variations with respect to the cross-sectional area of the unit cell. Throughout the optimization process, the actual values with the EIAP parameter sets are determined by using the General Utility Lattice Program (GULP)[44]. As the criteria to terminate the optimization process, the average error rate of the fitness function on all characteristics is considered to be less than 8%.

Table I lists all the parameters employed by our EIAP model. Note that our parametrization does not include S-S interactions as these occur beyond the cutoff limits considered by our force field. Nevertheless, we express most of the parameters to one or zero to mathematically express that the forces between sulphur atoms are null. Nevertheless, if the definition of these parameters is needed, users can choose the other parameters arbitrarily by accepting the β parameter as zero.

TABLE I. Optimized Tersoff-type EIAP parameters obtained by using the PSO method for the ZrS_3.

[1.5pt]	S-S	Zr-S	S-Zr
[1.1pt] A (eV)	6079.509429	6791.038544	6791.038544
B (eV)	3469.937384	2571.342251	2571.342251
λ_1 (Å^{-1})	4.097976	2.682439	2.682439
λ_2 (Å^{-1})	5.406911	2.262903	2.262903
λ_3 (Å^{-1})	1	3.220796	2.360710
n	1	16.561661	17.871640
β	0	3.025912e-6	3.785443e-6
c	1	61909.933731	52020.863988
d	1	11.669713	18.592590
h	1	-0.227712	-0.179199
R (Å)	2.40	3.40	3.40
D (Å)	0.10	0.20	0.20

Having defined each one of the interactions, we discuss now the optimization process. This process takes as input the cell vectors and phonon dispersion curves obtained with DFT and then optimizes the lattice constants of the unit cell and the phonon frequencies corresponding to the selected acoustical and optical vibrations using different wavelengths. Once the optimisation is finished, we show in Fig. 2 the phonon dispersion curves calculated from density functional theory (DFT) and the optimized potential parameters (EIAP), noting the good agreement for the lowest-lying frequency branches, which are the largest contributors to phonon transport. The phonon dispersion curves do not account for long-range electrostatic interactions. Sohier et al.[45] showed that when this is done properly for 2D materials: (i) the TO-LO splitting at the Γ point is suppressed and that (ii) at low $\mathbf{q}$-vectors the optical phonon branches depend linearly on the crystal momentum. The suppression of the TO-LO splitting, in practice, is achieved by not including the so-called non-analytical corrections in their common 3D formulation, as corroborated recently in a joint theoretical-experimental study[46]. Conversely, the linear dependence of the optical phonon energy at small $\mathbf{q}$-vectors requires an *ad hoc* implementation.[47] Nevertheless, we observe that the expected effect of this improved description of the optical phonons next to the Γ point on the estimate of the thermal conductivity is at most very small, but typically negligible. For instance, minimal differences have been found in the thermal conductivity of polar III-V semiconductors, such as GaAs or InP, upon adding the non-analytical corrections in the harmonic force constants.[48]

Using the parameters in Table I, we obtain for the unit cell

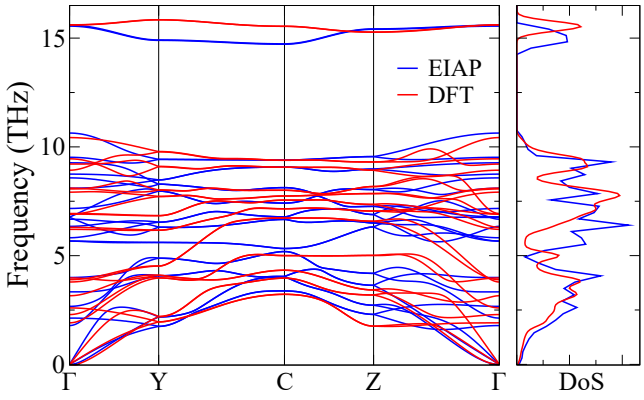

FIG. 2. Phonon dispersion curves obtained with the first-principles (DFT, red line), force-field-based calculations (EIAP, blue line) for the monolayer ZrS_3.

the lattice parameters a = 0.512 nm and b = 0.365 nm that are in excellent agreement with their counterparts obtained with DFT (a = 0.512 nm and b = 0.363 nm). In addition, we plot the variation of the system's total energy with respect to the cross sectional area of the unit cell in Fig. 3.

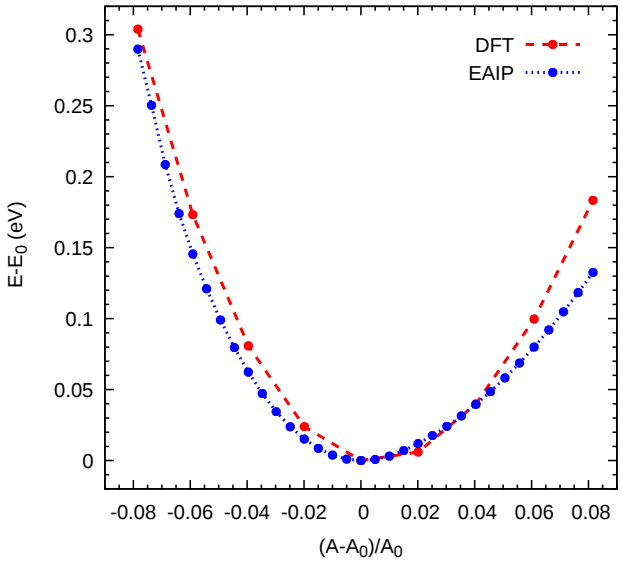

FIG. 3. Variation of the system's total energy E with first-principles (DFT in red) and force-field-based calculations (EIAP in blue) vs. the relative difference of the cross sectional area A of the unit cell for the ZrS_3 monolayer with respect to their corresponding values in equilibrium E_0 and A_0.

C. Non-equilibrium molecular dynamics

Once the parameters of the EIAP model are determined, we use the LAMMPS[49] MD code to calculate the thermal conductivities of single layers of ZrS_3 using the reversed non-equilibrium method[18]. In this method, a heat flux is induced along the x and y directions by removing and adding a fixed amount of energy e each time step in two narrows regions with a thickness 5 nm: the first one is located at x = 0 and y = 0 nm and is referred to as the hot reservoir, and the second slit is located at one half of the system's lengths L_x and L_y referred to as the cold reservoir. As the equations of motion are being integrated at constant volume and energy (NVE), the system's response is a temperature gradient dT/dx established along the heat flux direction between both reservoirs. Then, by using in all cases the same amount of heat flux q and assuming that non-linear effects in the heat transport can be neglected, the thermal conductivity can be computed using Fourier's law

$$q = \frac{e}{A} = -\kappa \frac{dT}{dx}, \tag{6}$$

where A is the cross section area of the ZrS_3 monolayer that has a thickness Δz = 0.898 nm taken from the experimental value of the interlayer separation[8] and a cross-section of $\Delta y \Delta z$ if the flux is applied along the x direction and $\Delta x \Delta z$ along the y axis. The value of Δx is 3.07 nm and Δy is 2.19 nm, which both are obtained by replicating the unit cell six times in the x and y directions, respectively.

The systems are then built replicating the unit cell $N_{rep,x}$ = 600, 800, 1000, and 1400 times in the x direction to compute the component κ_{xx} and $N_{rep,y}$ = 600, 800, 1200, and 2000 times in the y axis to calculate the component κ_{yy}, accounting for supercell sizes of up to 716.8 and 726 nm, respectively. Next, these layers are relaxed in two MD runs of 200 ps long each one with a timestep Δt of 0.5 x 10^{-3} ps: the first at 1 bar and 300 K (NPT); the second at constant volume and energy (NVE). Finally, we proceed with a third MD run where at each timestep we add 2 x 10^{-5} eV to the heat reservoir and subtract this exact same energy from its cold counterpart. During this NVE run, the equations of motion are integrated for 7.5 ns for the smallest and medium-sized systems and 20.0 ns for the two largest ones (i.e. those taking 6 x 1400 x 1 and 6 x 2000 x 1 replicas). The simulations times are long enough such that the temperature at the reservoirs is stabilized at around 50 % of the final simulation time. At this point we start computing the temperatures along the slab every 5 ps to obtain the thermal gradient. This gradient is determined by dividing the slab in $N_{rep,y} = N_{rep,x}/10$ domains, which usually contains nearly 500 atoms, a population large enough to define the temperature at each region j using the equipartition theorem for a 3D system

$$3N_j k_B T_j = \frac{1}{2} \sum_i m_i (\mathbf{v}_i - \mathbf{v}_j)^2, \tag{7}$$

where k_B is the Boltzmann constant, m_i is the mass of the i^{th} atom and $\mathbf{v}_i$ its the velocity vector and $\mathbf{v}_j$ is the velocity vector of the center of mass in each region that contains N_j particles.

D. Vibrational analysis

We also extract the vibrational density of states from ZrS_3 monolayers using classical MD with our interatomic potential

and compare it with that obtained employing ab initio molecular dynamics (AIMD). We calculate these densities of states as the Fourier transform of the velocity autocorrelation function $Z(t_n)$, which is computed as

$$Z(t_n) = \frac{1}{N_{at}} \sum_{n=0}^{N_{sim}} \sum_{i=1}^{Nat} \mathbf{v}_i(t_n) \cdot \mathbf{v}_i(t_0), \tag{8}$$

where $\mathbf{v}_i(t_n)$ is the velocity vector of the i^{th} atom at the initial at time t_n, N_{at} is the number of atoms in the system, and N_{sim} is the number of integration steps with a length Δt = 0.5 x 10^{-3} ps for the AIMD and MD simulations.

For ab initio MD, we change the following DFT parameters from the scheme used to obtain the phonon dispersion curves. We use a less strict threshold of 1 x 10^{-5} eV (i.e., nonetheless 1.04 x 10^{-7} eV/atom) for self-consistency solution of the wavefunction to make it several times faster. In addition, due to the high cost of running AIMD simulations, the size of the monolayer is restricted to 3 x 4 cells in the x and y directions, respectively. The monolayer is first relaxed at 1 bar and 300 K using a NPT scheme for 2 x 10^4 steps. After this 10-ps relaxation, the velocity autocorrelation function is calculated at each integration step, upon which the atomic trajectories are determined at constant volume at 300 K for another 10 ps. For the MD simulation, the monolayers have two sizes: 3 x 4 to compare directly with ab initio results and 10 x 14 to evaluate any size effects of our interatomic potential on the frequencies. In these classical runs, the two monolayers are relaxed at 1 bar and 300 K during 200 ps to then collect the autocorrelation function at each time step using a NVT simulation at 300 K for 7.5 ns.

III. RESULTS AND DISCUSSION

We start presenting our non-equilibrium MD results with the thermal gradient obtained for a representative case. Figure 4 illustrates the thermal gradient along the y direction across the system made with 6 x 2000 replicas of the unit cell accompanied by the linear fits that are taken to obtain thermal gradients in absolute values of 0.171 K/nm between in left-hand-side region between the cold and hot reservoirs and 0.159 K/nm on its right-hand-side partner. For this case and the rest of them, we take the average of both gradients and plug it into eq. 6 to determine a value of 26.75 W m^{-1} K^{-1} for κ_{yy} with a length L_y = 738.91 nm. This averaging procedure yields a value of κ_{xx} = 19.45 W m^{-1} K^{-1} for L_x = 720.31 nm.

The next step in the non-equilibrium method,[19,50] is to plot the reciprocal values of κ_{xx} and κ_{yy} *vs.* the lengths L_x and L_y to remove the contribution of boundary scattering by extrapolating the behavior of the thermal conductivity for infinitely large cells. Fig. 5 shows the linear relationships between $\frac{1}{\kappa_{xx}}$ with decreasing $\frac{1}{L_x}$ and $\frac{1}{\kappa_{yy}}$ with decreasing $\frac{1}{L_y}$ at 300 K. Both sets are then fitted according to

$$\frac{1}{\kappa_{ii}} = \frac{1}{\kappa_{ii}^{\infty}} \left(\frac{\lambda}{L_i} + 1 \right), \tag{9}$$

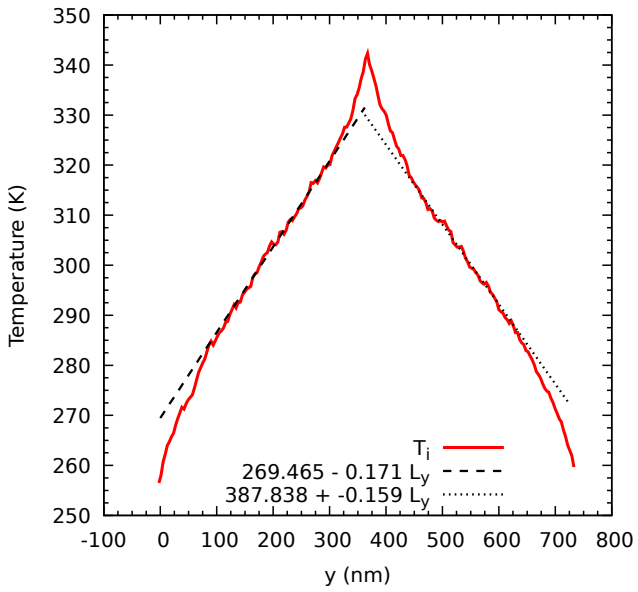

FIG. 4. Temperatures T_i (in red line) computed in 200 regions for a monolayer replicated 6x2000x1 times along y-direction with a slab relaxed at 300 K

. Two linear fittings(in dashed and dotted lines) are made on both intermediate regions separating the cold and hot reservoirs.

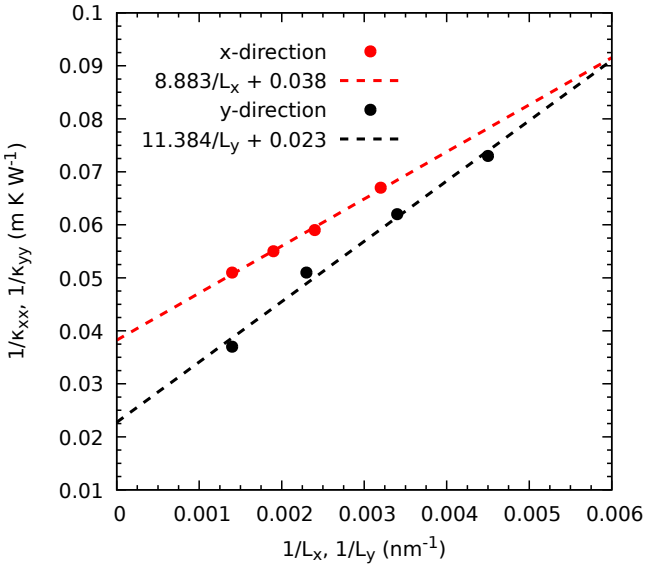

FIG. 5. Reciprocal values of the thermal conductivity components κ_{xx} and κ_{yy} vs. longest lengths L_x and L_y at 300 K.

where λ is the effective phonon mean free path and $\kappa_{ii,\infty}$ is the component of the thermal conductivity for a given direction i. Both linear fittings predict that κ_{xx} = 25.69 W m^{-1} K^{-1} and κ_{yy} = 42.38 W m^{-1} K^{-1}, yielding an anisotropic ratio κ_{yy}/κ_{xx} of 1.65. These values compare very well with those obtained using first-principles simulations: κ_{xx} = 25.68 W m^{-1} K^{-1} and κ_{yy} = 40.72 W m^{-1} K^{-1}, which result in an anisotropic

ratio $\frac{\kappa_{yy}}{\kappa_{xx}}$ = 1.54 using a mesh of 55 x 55 x 1 **q**-points in the reciprocal space to sample the Brillouin zone. We find that while the prediction for the x-component with DFT is excellent, while the discrepancy in the y axis is only -4.06 %, which can be attributed to two factors: first, the inherent error between the lowest-lying phonon branches along the path Γ-Z shown in Fig. 2; second, the unavoidable error when projecting the thermal conductivity in the limit of $1/L_x$ and $1/L_y \rightarrow 0$. Nonetheless, we find that this second source of discrepancy with DFT is reasonable as we find that κ_{xx} reaches 73.13 % of its projected value with L_x = 720.39 nm and κ_{yy} attains 70.22% with L_y = 738.74 nm. These contributions compare well with those given by our first-principles scheme, which predicts that with these lengths approximately 56% of κ_{xx} and 60% of κ_{yy} are reached as shown in Fig. 6.

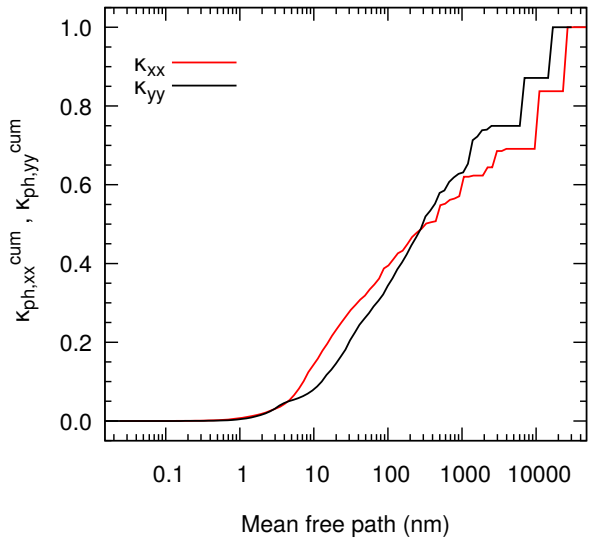

FIG. 6. Normalized cumulative function of the components of the tensor of the lattice thermal conductivity $\kappa^{cum}_{ph,xx}$ and $\kappa^{cum}_{ph,yy}$ as a function of the phonon mean free path from first-principles calculations at 300 K .

Note though that DFT results are generally subject to several choices such as the exchange-correlation functional,[51] the thresholds for the energy in the self-consistency solution of wavefunction and for the forces in the geometry optimization, and the number **q**-points[23]. In particular, this number produces some variance in the thermal conductivity components. For instance, κ_{xx} is equal to 22.47 W m^{-1} K^{-1} with 50 **q**-points and to 24.81 W m^{-1} K^{-1} with 60 **q**-points, while the corresponding values for κ_{yy} are 39.73 and 38.28 W m^{-1} K^{-1}. Although both magnitudes are stabilized between 50 and 60 **q**-points, their oscillations in this range are high enough to increase or reduce the discrepancy with our MD results. Furthermore, another source discrepancy emerges from the role of scattering from isotopic disorder included by default in our first-principles methodology[37]. Although the inclusion of these isotopic disorder is made by default in the almaBTE code, we expect a little contribution towards the discrepancy with MD values.

Nevertheless, the comparison between both techniques at this point lacks a critical factor: temperature , which brings the influence of lattice expansion and phonon-phonon scattering with thermal vibrations. For the lattice expansion, note that our first-principles computations depend on the DFT matrices of second and third order force constants calculated at zero Kelvin with a = 0.512 nm and b = 0.363 nm, while in our MD computations the corresponding averaged values of a are 0.513, 0.514, 0.516, and 0.518 nm for the monolayer made of 400x6x1 unit cells, while for b are 0.367, 0.368, 0.369, 0.370 nm and using the for the system composed of 6x400x1 unit cells at 100, 200, 300, and 400 K. In both cases, the difference between MD and freezed values of the lattice constants obtained are up to 0.74% for a and 2.18% for b, which indicates that lattice expansion with increasing temperature is a non-negligible factor that make these two force constants differ in DFT and MD differ, and hence, the thermal conductivity obtained with Eq. 2. For the phonon-phonon scattering with thermal vibrations, the phonon frequencies displayed in Fig. 2 indicate that when temperature is imposed the peaks of the associated density of states degenerate, perturbing the weight of acoustic and optical frequencies towards thermal transport in Eq. 2, which adds an another source of discrepancy between the results found with first-principles and classical MD.

Therefore, our investigation about this discrepancy brings us now to study the vibrational spectra of ZrS_3 monolayers collected from both techniques. However, we are here interested in finding how our interatomic potential reproduces the vibrational peaks in range of temperatures between 10 K and 400 K with ab initio and classical MD with a monolayer built with 3x4 unit cells. Figure 7(a) shows that the AIMD vibrational spectrum at 10 K have the strongest peak near 2 THz, which coincides with the frequency ranges that are occupied by the lowest-lying phonon branches collected at T = 0 K shown in Fig. 2. Fig. 7(a) also shows other weaker peaks up to nearly 11 THz and a phonon gap roughly sitting in an interval delimited by this frequency and 13.75 THz. At this point and near 15 THz, we collect two weak optical signals, in good agreement with the phonon dispersions. However, as the temperature is increased in AIMD, the strength of all these peaks is dramatically changed. For instance, although the first peak persists at 100 K, it vanishes for higher temperatures, while intermediate signals between 6 and 8 THz clearly stand out. It is remarkable that at 200 K and above, our AIMD simulations show a stronger optical peak, consequently defining a clearer phonon gap. In contrast, only a few of these AIMD features are reproduced by its classical MD counterparts depicted in Fig. 7(b). For example, MD barely reproduces the AIMD mark at 2 THz; which needs higher temperatures to recover. In addition, although the phonon gap virtually disappears for all temperatures, we find that the optical vibrations are displayed for 200 K and above, in agreement with our quantum mechanical spectra. Finally, we assess the influence of the system size on these MD densities of states with a much larger monolayer made of 10x14 unit cells. The spectra in Fig. 7(c) shows that although most of the optical peaks are washed away, the signals up to 6 THz are still well defined.

Finally, we evaluate the values of κ_{xx} and κ_{yy} as a func-

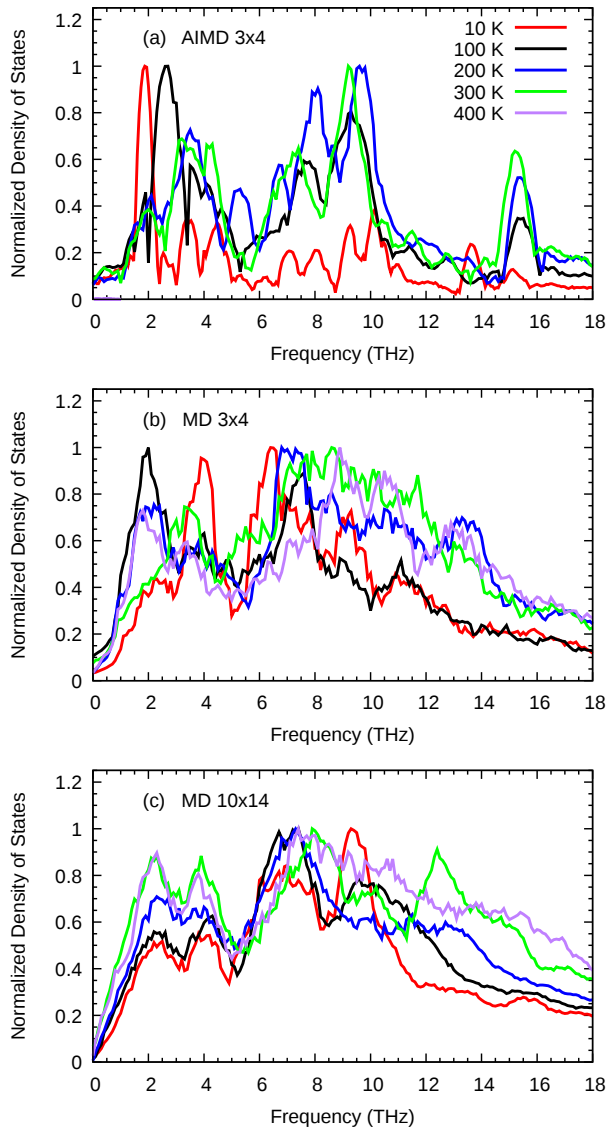

FIG. 7. Normalized VDOS at 10, 100, 200, 300, and 400 K collected with ab initio molecular dynamics (AIMD) using monolayers made by replicating the unit cells 3x4 (a), and classical MD with 3x4 (b) and 10x14 replicas (c).

tion of temperature predicted with our NEMD method and compare them with those computed with first-principles lattice dynamics. Figure 8 shows the decrease of κ_{xx} and κ_{yy} with increasing temperature between 100 and 400 K. The first-principles components strongly reduce with temperature, starting with κ_{xx} = 97.24 W m^{-1} K^{-1} and κ_{yy} = 150.96 W m^{-1} K^{-1} at 100 K and shrinking down to 18.30 and 28.21 W m^{-1} K^{-1} at 400 K, respectively. This decrease indicates that Umklapp processes are the dominant scattering mechanism, a feature also found in TiS_3 monolayers.[17] The NEMD counterparts also exhibit a decrease but not as pronounced as κ_{xx} decreases from 29.42 W m^{-1} K^{-1} at 100 K to 26.28 W m^{-1} K^{-1} at 400 K and κ_{yy} from 49.34 to 33.41 W m^{-1} K^{-1}. We believe that this much lower sensitivity to temperature is caused by several factors: first, anharmonic effects with fourth order or higher not taken into account by our first-principles scheme[52–54]; second, strain effects produced by the monolayer buckling, which we have shown that enhance phonon scattering in ZrS_3 monolayers that ultimately reduce the thermal conductivity by up five-fold[23]; third, the well-known differences in the phonon distributions between molecular dynamics and first-principles descriptions, evidenced in the vibrational spectra illustrated in Fig. 7; fourth, classical trajectories cannot be used to determine thermal conductivities at low temperatures because quantum effects in the nuclear motion are neglected by our EIAP. Therefore, the disagreement between DFT and MD conductivities below 200 K is expected as, in principle, our results are accurate only at sufficiently high temperatures, where the Maxwell-Boltzmann distribution can be assumed to be a good approximation to Bose-Einstein statistics for phonon populations. However, even if this approximation cannot be assumed and hence quantum effects are expected to be significant below the Debye temperature, thermal conductivities computed with MD agree well with the available experimental data. A number of studies have investigated this feature in bulk-like and 2D materials in a number of studies,[55–57] which has been attributed to the compensation of two opposite errors provided by classical simulations: shorter phonon lifetimes and larger single-phonon contributions to heat capacity than their quantum counterparts.

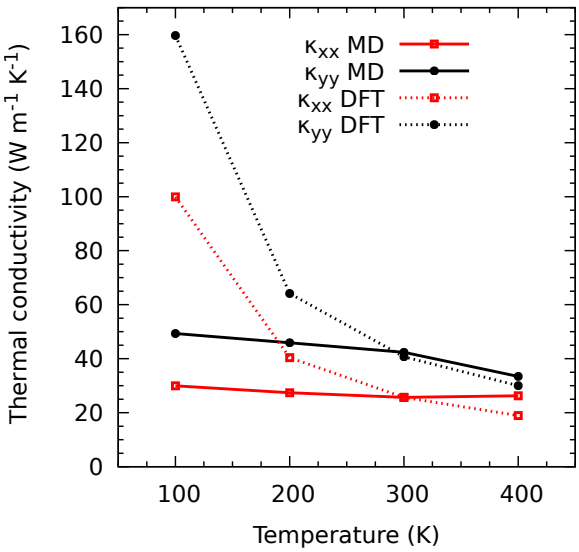

FIG. 8. Thermal conductivities κ_{xx} and κ_{yy} calculated with NEMD and DFT vs. temperature.

IV. CONCLUSIONS

In summary, this manuscript presents a new interatomic potential that reproduces the phonon transport properties of zirconium trisulphide monolayers predicted with first-principles

lattice dynamics. This work is intended to compare the thermal conductivity obtained with our potential with that computed with a standard first-principles methodology, which is based on DFT and a solution of the Boltzmann Transport Equation beyond the relaxation time approximation (RTA). This methodology treats anharmonicity up to the third order and provides good agreement with available experimental results on several 2D materials.[58,59]. We have employed the non-equilibrium method to predict the components κ_{xx} and κ_{yy} of the thermal conductivity tensor. Our molecular dynamics scheme predicts at 300 K κ_{xx} is 25.69 W m^{-1} K^{-1} and κ_{yy} = 42.38 W m^{-1} K^{-1}, which both agree well with their corresponding first-principles counterparts of 25.68 and 40.72 W m^{-1} K^{-1}. We believe that the small disagreement in the x-direction is caused by inherent discrepancy between the lowest-lying phonon branches along the path [0, 0, 0] $\rightarrow$ [0, 1/2, 0] and the unavoidable uncertainty when projecting the thermal conductivity in the limit of $1/L_x$ and $1/L_y \rightarrow 0$.

Additionally, we extract the vibrational density of states of the monolayers with classical and ab initio molecular dynamics. We find that most of the ab initio peaks are well reproduced by our interatomic potential, which naturally tends to generate a noisier signals. However, the optical peaks in the classical spectra are completely degenerated, which we think is caused by the sinusoidal movement of the monolayer that could be inhibited by the smaller computational cell that we have had to use in AIMD. Finally, we test our interatomic potential by computing κ_{xx} and κ_{yy} as a function of temperature between 100 and 400 K. Our calculations indicate that both magnitudes shows a less pronounced decrease with increasing temperature than that shown by those determined with first-principles lattice dynamics. A feature that suggests again that the influence of the effects caused by anharmonicity with orders higher than three, the monolayer buckling that induces a strain to the ZrS_3 monolayers, and the unsuitability of the approximation of classical ionic trajectories at low temperature in MD.

V. SUPPLEMENTARY INFORMATION

We provide as a supplementary information the parameters of our interatomic potential for its in LAMMPS.

ACKNOWLEDGMENTS

We acknowledge the financial received from the European Union's Horizon 2020 research and innovation programme under grant agreement No 793726 (TELIOTES - Thermal and electronic transport in inorganic-organic thermoelectric superlattices) and the support of The Supercomputing Center of Galicia (CESGA) where the calculations have been made. We also acknowledge financial support by the Ministerio de Economía, Industria y Competitividad (MINECO) under grant FEDER-MAT2017-90024-P and the Severo Ochoa Centres of Excellence Program under Grant SEV-2015-0496 and by the Generalitat de Catalunya under grant no. 2017 SGR 1506. The authors acknowledge also the fruitful discussions with Dr. Jesús Carrete Montaña at TU Wien. The authors declare no conflict of interest.

DATA AVAILABILITY

The data that support the findings of this study are available from the corresponding author upon reasonable request.

[1] K. S. Novoselov, A. K. Geim, S. V. Morozov, D. Jiang, Y. Zhang, S. V. Dubonos, I. V. Grigorieva, and A. A. Firsov, "Electric field effect in atomically thin carbon films," Science **306**, 666–669 (2004).

[2] K. S. Novoselov, D. Jiang, F. Schedin, T. J. Booth, V. V. Khotkevich, S. V. Morozov, and A. K. Geim, "Two-dimensional atomic crystals," Proc. Natl. Acad. Sci. USA **102**, 10451–10453 (2005).

[3] M. Y. Han, B. Özyilmaz, Y. Zhang, and P. Kim, "Energy band-gap engineering of graphene nanoribbons," Phys. Rev. Lett. **98**, 206805 (2007).

[4] A. A. Balandin, S. Ghosh, W. Bao, I. Calizo, D. Teweldebrhan, F. Miao, and C. N. Lau, "Superior thermal conductivity of single-layer graphene," Nano Lett. **8**, 902–907 (2008).

[5] M. Xu, T. Liang, M. Shi, and H. Chen, "Graphene-like two-dimensional materials," Chem. Rev. **113**, 3766–3798 (2013).

[6] A. C. Ferrari, F. Bonaccorso, V. Fal'Ko, K. S. Novoselov, S. Roche, P. Bøggild, S. Borini, F. H. Koppens, V. Palermo, N. Pugno, *et al.*, "Science and technology roadmap for graphene, related two-dimensional crystals, and hybrid systems," Nanoscale **7**, 4598–4810 (2015).

[7] L. Brattas and A. Kjekshus, "On the properties of compounds with the $ZrSe_3$ type structure," Acta Chem. Scand. **26**, 3441–3449 (1972).

[8] S. Furuseth, L. Brattas, and A. Kjekshus, "Crystal structures of TiS_3, ZrS_3, $ZrSe_3$, $ZrTe_3$, HfS_3 and $HfSe_3$," Acta Chem. Scand. **29**, 623 (1975).

[9] J. O. Island, A. J. Molina-Mendoza, M. Barawi, R. Biele, E. Flores, J. M. Clamagirand, J. R. Ares, C. Sánchez, H. S. van der Zant, R. D'Agosta, *et al.*, "Electronics and optoelectronics of quasi-1D layered transition metal trichalcogenides," 2D Mater. **4**, 022003 (2017).

[10] Y. Jin, X. Li, and J. Yang, "Single layer of MX_3 (M = Ti, Zr; X = S, Se, Te): a new platform for nano-electronics and optics," Phys. Chem. Chem. Phys. **17**, 18665–18669 (2015).

[11] Y. Saeed, A. Kachmar, and M. A. Carignano, "First-principles study of the transport properties in bulk and monolayer MX_3 (M = Ti, Zr, Hf; X = S, Se,) compounds," J. Phys. Chem. C **121**, 1399–1403 (2017).

[12] N. V. Morozova, I. V. Korobeinikov, K. V. Kurochka, A. N. Titov, and S. V. Ovsyannikov, "Thermoelectric properties of compressed titanium and zirconium trichalcogenides," J. Phys. Chem. C **122**, 14362–14372 (2018).

[13] F. Saiz and R. Rurali, "Strain engineering of the electronic and thermoelectric properties of titanium trisulphide monolayers," Nano Express (2020).

[14] L. Musland and E. Flage-Larsen, "Thermoelectric effect in superlattices; applicability of coherent and incoherent transport models," Comp. Mat. Sci. **153**, 88 – 96 (2018).

[15] C. da Silva, F. Saiz, D. A. Romero, and C. H. Amon, "Coherent phonon transport in short-period two-dimensional superlattices of graphene and boron nitride," Phys. Rev. B **93**, 125427 (2016).

[16] P. Torres, F. X. Alvarez, X. Cartoixà, and R. Rurali, "Thermal conductivity and phonon hydrodynamics in transition metal dichalcogenides from first-principles," 2D Mater. **6**, 035002 (2019).

[17] F. Saiz, J. Carrete, and R. Rurali, "Anisotropic thermal conductivity in few-layer and bulk titanium trisulphide from first principles," Nanomaterials **10**, 704 (2020).

[18] F. Müller-Plathe, "A simple nonequilibrium molecular dynamics method for calculating the thermal conductivity," J. Chem. Phys. **106**, 6082–6085 (1997).

[19] P. K. Schelling, S. R. Phillpot, and P. Keblinski, "Comparison of atomic-level simulation methods for computing thermal conductivity," Phys. Rev. B **65**, 144306 (2002).

[20] M. S. Green, "Markoff random processes and the statistical mechanics of time-dependent phenomena. ii. irreversible processes in fluids," J. Chem. Phys. **22**, 398–413 (1954).

[21] R. Kubo, M. Yokota, and S. Nakajima, "Statistical-mechanical theory of irreversible processes. ii. response to thermal disturbance," J. Phys. Soc. Jap. **12**, 1203–1211 (1957).

[22] F. Saiz, C. da Silva, and C. H. Amon, "Prediction of thermal conductivity of two-dimensional superlattices of graphene and boron nitride by equilibrium molecular dynamics," in *ASME International Mechanical Engineering Congress and Exposition*, Vol. 57502 (American Society of Mechanical Engineers, 2015) p. V08BT10A026.

[23] F. Saiz, J. Carrete, and R. Rurali, "Optimisation of the thermoelectric efficiency of zirconium trisulphide monolayers through unixial and biaxial strain," Nanoscale Adv. **2**, 5352–5361 (2020).

[24] G. Kresse and J. Hafner, "Ab initio molecular dynamics for liquid metals," Phys. Rev. B **47**, 558–561 (1993).

[25] G. Kresse and J. Hafner, "Ab initio molecular-dynamics simulation of the liquid-metal–amorphous-semiconductor transition in germanium," Phys. Rev. B **49**, 14251–14269 (1994).

[26] G. Kresse and J. Furthmüller, "Efficiency of ab-initio total energy calculations for metals and semiconductors using a plane-wave basis set," Comp. Mat. Sci. **6**, 15 – 50 (1996).

[27] G. Kresse and J. Furthmüller, "Efficient iterative schemes for ab initio total-energy calculations using a plane-wave basis set," Phys. Rev. B **54**, 11169–11186 (1996).

[28] J. P. Perdew, K. Burke, and M. Ernzerhof, "Generalized gradient approximation made simple," Phys. Rev. Lett. **77**, 3865–3868 (1996).

[29] P. E. Blöchl, "Projector augmented-wave method," Phys. Rev. B **50**, 17953 (1994).

[30] G. Kresse and D. Joubert, "From ultrasoft pseudopotentials to the projector augmented-wave method," Phys. Rev. B **59**, 1758–1775 (1999).

[31] A. Togo and I. Tanaka, "First principles phonon calculations in materials science," Scr. Mater. **108**, 1–5 (2015).

[32] W. Li, N. Mingo, L. Lindsay, D. A. Broido, D. A. Stewart, and N. A. Katcho, "Thermal conductivity of diamond nanowires from first principles," Phys. Rev. B **85**, 195436 (2012).

[33] W. Li, J. Carrete, N. A. Katcho, and N. Mingo, "ShengBTE: a solver of the Boltzmann transport equation for phonons," Comp. Phys. Comm. **185**, 1747–1758 (2014).

[34] J. Carrete, B. Vermeersch, A. Katre, A. van Roekeghem, T. Wang, G. K. Madsen, and N. Mingo, "almabte: A solver of the space-time dependent boltzmann transport equation for phonons in structured materials," Comp. Phys. Comm. **220**, 351–362 (2017).

[35] W. Li, L. Lindsay, D. A. Broido, D. A. Stewart, and N. Mingo, "Thermal conductivity of bulk and nanowire $Mg_2Si_xSn_{1-x}$ alloys from first principles," Phys. Rev. B **86**, 174307 (2012).

[36] P. Torres, A. Torelló, J. Bafaluy, J. Camacho, X. Cartoixà, and F. X. Alvarez, "First principles kinetic-collective thermal conductivity of semiconductors," Phys. Rev. B **95**, 165407 (2017).

[37] S. Tamura, "Isotope scattering of dispersive phonons in ge," Phys. Rev. B **27**, 858–866 (1983).

[38] J. Carrete, W. Li, L. Lindsay, D. A. Broido, L. J. Gallego, and N. Mingo, "Physically founded phonon dispersions of few-layer materials and the case of borophene," Mat. Res. Lett. **4**, 204–211 (2016).

[39] J. Tersoff, "New empirical approach for the structure and energy of covalent systems," Phys. Rev. B **37**, 6991–7000 (1988).

[40] Y. Karaaslan, H. Yapicioglu, and C. Sevik, "Assessment of Thermal Transport Properties of Group-III Nitrides: A Classical Molecular Dynamics Study with Transferable Tersoff-Type Interatomic Potentials," Phys. Rev. Appl. **13**, 034027 (2020).

[41] Y. Karaaslan, H. Yapicioglu, and C. Sevik, "Optimizing the Thermal Transport Properties of Single Layer (2D) Transition Metal Dicalcogenides (TMD)," Eskişehir Technical University Journal of Science and Technology A - Applied Sciences and Engineering **20**, 373 – 392 (2019).

[42] A. Kandemir, H. Yapicioglu, A. Kinaci, T. Çağın, and C. Sevik, "Thermal transport properties of MoS_2 and $MoSe_2$ monolayers," Nanotech. **27**, 055703 (2016).

[43] A. Mobaraki, A. Kandemir, H. Yapicioglu, O. Gülseren, and C. Sevik, "Validation of inter-atomic potential for WS_2 and WSe_2 crystals through assessment of thermal transport properties," Comp. Mat. Sci. **144**, 92 – 98 (2018).

[44] J. D. Gale and A. L. Rohl, "The general utility lattice program (gulp)," Molecular Simulation **29**, 291–341 (2003).

[45] T. Sohier, M. Gibertini, M. Calandra, F. Mauri, and N. Marzari, "Breakdown of optical phonons' splitting in two-dimensional materials," Nano letters **17**, 3758–3763 (2017).

[46] M. De Luca, X. Cartoixa, D. Indolese, J. Martín-Sánchez, K. Watanabe, T. Taniguchi, C. Schoenenberger, R. Trotta, R. Rurali, and I. Zardo, "Experimental demonstration of the suppression of optical phonon splitting in 2d materials by raman spectroscopy," 2D Materials (2020).

[47] P. Giannozzi, S. Baroni, N. Bonini, M. Calandra, R. Car, C. Cavazzoni, D. Ceresoli, G. L. Chiarotti, M. Cococcioni, I. Dabo, *et al.*, "Quantum espresso: a modular and open-source software project for quantum simulations of materials," Journal of physics: Condensed matter **21**, 395502 (2009).

[48] M. Raya-Moreno, R. Rurali, and X. Cartoixà, "Thermal conductivity for iii-v and ii-vi semiconductor wurtzite and zinc-blende polytypes: The role of anharmonicity and phase space," Physical Review Materials **3**, 084607 (2019).

[49] S. Plimpton, "Fast parallel algorithms for short-range molecular dynamics," J. Comp. Phys. **117**, 1–19 (1995).

[50] Y. Hong, J. Zhang, and X. C. Zeng, "Thermal conductivity of monolayer $MoSe_2$ and MoS_2," J. Phys. Chem. C **120**, 26067–26075 (2016).

[51] A. Taheri, C. Da Silva, and C. H. Amon, "Effects of biaxial tensile strain on the first-principles-driven thermal conductivity of buckled arsenene and phosphorene," Phys. Chem. Chem. Phys. **20**, 27611–27620 (2018).

[52] S.-Y. Yue, X. Zhang, G. Qin, S. R. Phillpot, and M. Hu, "Metric for strong intrinsic fourth-order phonon anharmonicity," Physical Review B **95**, 195203 (2017).

[53] T. Feng, X. Yang, and X. Ruan, "Phonon anharmonic frequency shift induced by four-phonon scattering calculated from first principles," Journal of Applied Physics **124**, 145101 (2018).

[54] X. Gu, Z. Fan, H. Bao, and C. Zhao, "Revisiting phonon-phonon scattering in single-layer graphene," Physical Review B **100**, 064306 (2019).

[55] O. N. Bedoya-Martinez, J.-L. Barrat, and D. Rodney, "Computation of the thermal conductivity using methods based on classical and quantum molecular dynamics," Physical Review B **89**, 014303 (2014).

[56] D. Singh, J. Y. Murthy, and T. S. Fisher, "Mechanism of thermal conductivity reduction in few-layer graphene," Journal of Applied Physics **110**, 044317 (2011).

[57] C. Caddeo, C. Melis, A. Ronchi, C. Giannetti, G. Ferrini, R. Rurali, L. Colombo, and F. Banfi, "Thermal boundary resistance from transient nanocalorimetry: A multiscale modeling approach," Physical Review B **95**, 085306 (2017).

[58] G. Fugallo, A. Cepellotti, L. Paulatto, M. Lazzeri, N. Marzari, and F. Mauri, "Thermal conductivity of graphene and graphite: collective excitations and mean free paths," Nano letters **14**, 6109–6114 (2014).

[59] P. Torres, F. X. Alvarez, X. Cartoixà, and R. Rurali, "Thermal conductivity and phonon hydrodynamics in transition metal dichalcogenides from first-principles," 2D Materials **6**, 035002 (2019).